Supplement: Modelling the Life–Cycle Impacts of Air Pollution on Tropospheric Ozone and Methane

Contents

S1. Emission temporal profiles

Our temporal distributions for emissions profiles are derived using sectoral-resolved emissions from EDGAR v4.3.2 and separate temporal profiles (Crippa *et al*., 2020). They are resolved diurnally (every hour), by day-of-the-week (weekday, Saturday, and Sunday), and by month for the following emission sectors: agricultural waste burning, energy for buildings, fugitive emissions from refining, fuel exploitation, off-road transport, road transport, power generation, and combustion for manufacturing (see Figure S1). Our derived temporal profiles are a linear combination of the EDGAR sector-specific temporal profiles, and are applied equally to all KORUS v5 emissions (Woo *et al*., 2020) in each grid-cell.

In each model grid-cell, we estimate a single, fractional contribution of the eight emission sectors to the grid-cell emissions; these weightings are used to average the EDGAR temporal profiles over the sectors. The sector contributions are computed as the EDGAR sector-to-total emission ratio (kg m^{-2} s^{-1}) summed over the inventoried air pollutants (NO_x, CO, and 25 VOCs; see Table S1 for totals), but with the emission densities weighted by the approximate inverse lifetimes of the species in the BL. The reactivity weightings ensure our calculated diurnal emission cycles represent the sectors in proportion to their influence on the BL-RL model chemistry.

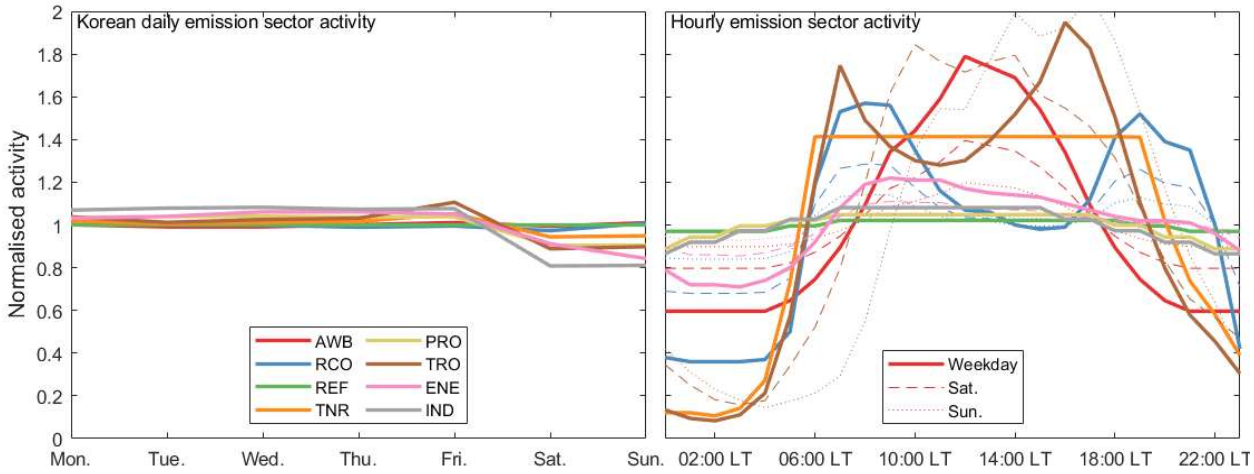

Figure S1: Days of the week (left) and hours of the day (right) temporal scale factors for EDGAR v4.3.2 emissions for the month of May. *The sectors are denoted as follows: AWB (agricultural waste burning), RCO (energy for buildings), REF (fugitive emissions from refining), TNR (off-road transport, i.e., rail, shipping, aircraft landing & take-off), PRO (fuel exploitation), TRO (road transportation), ENE (power generation), and IND (combustion for manufacturing). Solid, dashed, and dotted lines in the hourly profiles (right) indicate weekday, Saturday, and Sunday diurnal cycles respectively. Local time for all cells is Korean Standard Time.*

Table S1: Total South Korean emission rates and reactivity lifetimes used to derive our emission temporal scale factors.

Emitted Species (SAPRC ID)	EDGAR ID	KORUS v5 flux (kg hr^{-1})	EDGAR flux (kg hr^{-1})	Lifetime (hr)	1-hr decay fraction
CO	CO	20200	33200	2100	0.000
NO	NO_x	85300	143000	6.0	0.154
NO_2		17900			
Ethane (ALK1)	VOC02	3400	1400	3000	0.000
Propane (ALK2)	VOC03	3900	8440	560	0.002
n-Butane (ALK3)	VOC04	5300	5300	250	0.004
n-Pentane (ALK4)	VOC05	65000	719	140	0.007
n-Hexane (ALK4)	VOC06	16000	22000	100	0.010
n-Heptane (ALK5)				80	0.012
Ethene	VOC07	7690	3750	43	0.023
Propene (OLE1)	VOC08	4100	1470	9.0	0.105
Isoprene	VOC10	650	16	3.8	0.231
Butadiene (OLE2)	VOC12	5400	3520	6.2	0.149
Benzene (ARO1)	VOC13	33000	3170	460	0.002
Toluene (ARO1)	VOC14		4710	95	0.010
m-Xylene (ARO2)	VOC15	17000	5560	24	0.041
1,2,4-Trimethylbenzene (ARO2)	VOC16		564	17	0.057
Cresols	VOC17	100	4590	12	0.080
HCHO	VOC21	990	308	6.6	0.141
Acetaldehyde	VOC22	560	564	27	0.036
Propionaldehyde (RCHO)		300		13	0.074
Methylglyoxal		90		2.1	0.379
Benzaldehyde		30		33	0.030
Diacetyl		30		1.0	0.632
Acetone	VOC23	340	2560	71	0.014
Methyl ethyl ketone		570		99	0.010

South Korean emissions from KORUS v5 and EDGAR v4.3.2 are shown as sums over the BL-RL model domain for the month of May. Named species in the model are represented by both explicit and lumped categories, e.g., "ALK1" in KORUS v5, and "VOC06" in EDGAR. KORUS v5

fluxes are converted from mol s^{-1} to kg hr^{-1} for comparison with EDGAR using the masses of the representative "emitted species" in our modelling system. EDGAR emission fluxes were partitioned into sectors, scaled by the 1-hr decay fractions, then used as weightings to estimate the sector activity fraction in each terrestrial BL-RL grid-cell. The reactivity scalings are computed from OH rate constants in MCM v3.3.1 (Bloss et al., 2005; Jenkin et al., 1997; Jenkin et al., 2003; Jenkin et al., 2015; Saunders et al., 2003) using [OH] = 5 x 10^5 molec cm^{-3} and temperature = 288 K. In each grid-cell, the sector activities are used as weightings to average the sector-based temporal profiles shown in Figure S1.

S2. Model-observation comparison

Table S2 and Figures S2-S6 compare O_3, CO, and NO_x mole fractions in the "boundary layer-residual layer" (BL-RL) modelling stage, resolved as mixed BL column values, with NIER surface site data gridded to model resolution (0.1°x0.1°, hourly). Our comparisons are decomposed into four time periods characterised according to meteorology by Peterson et al., 2019: dynamic (01-16 May), anticyclone (17-22 May), transport (25-31 May), and rex-block (01-07 June). Figure S7 shows the geography of NASA DC-8 sampling during the KORUS-AQ mission, as used for model-observation comparison in the "plume" (PL) modelling stage.

Table S2: Model vs. observation performance metrics in the South Korean boundary layer (BL).

Meteorological Phase	Mean daytime bias (ppb)	Correlation (Pearson-*r*)	Model daytime max (ppb)	Obs. daytime max (ppb)	Model daytime min (ppb)	Obs. daytime min (ppb)
O_3						
Dynamic	21.6	0.58	79.5	64.3	59.5	32.1
Anticyclone	-0.8	0.78	87.1	95.8	51.0	52.0
Transport	-1.4	0.75	98.9	101.2	48.2	47.5
Rex block	21.6	0.74	111.0	83.2	61.5	39.0
CO						
Dynamic	-136.8	0.35	232.8	571.7	114.1	132.9
Anticyclone	-126.3	0.26	623.1	799.4	119.2	151.1
Transport	-236.4	0.28	525.5	808.4	117.3	194.6
Rex block	-123.7	0.30	449.2	692.4	115.3	123.8
NO_x						
Dynamic	-16.7	0.54	41.8	45.3	0.5	10.1
Anticyclone	-9.4	0.50	89.5	57.6	1.5	10.6
Transport	-9.7	0.53	93.9	57.5	1.6	11.9
Rex block	-12.5	0.51	71.8	51.5	1.3	9.0

Model data are BL column values from the BL-RL model. Data were sampled in grid-cells observed by at least five effective NIER sites, during the full days defined by the meteorological phases (see text in Section 4). Pearson's correlation coefficients were computed over the full diurnal cycles while mean daytime bias (model minus observation), daytime max, and daytime min columns were sampled during the period from 13:00-17:00 LT. Daytime maxes and mins were computed on individual days during the phases, then averaged over those meteorological stages.

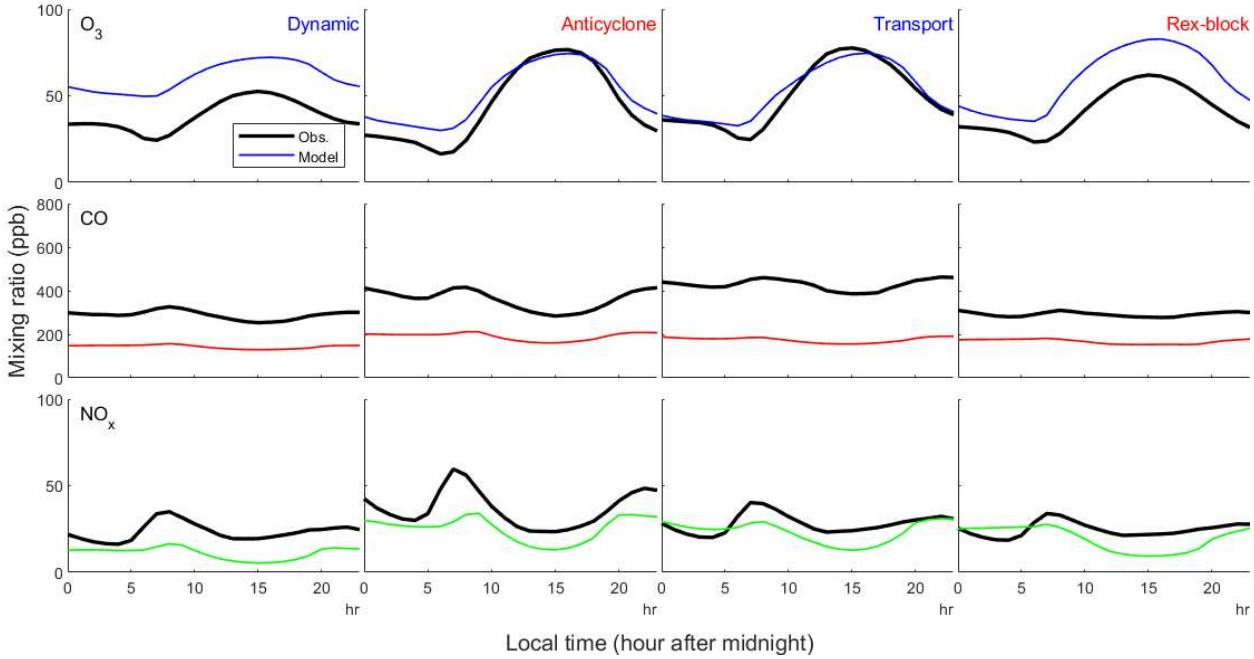

Figure S2: Mean diurnal cycles of surface observations (black lines) and model output (Coloured lines) for O_3 (top), CO (middle), and NO_x (bottom). *All data were sampled in grid-cells observed by at least five effective NIER sites. Diurnal averages were sampled separately within the meteorological stages as described in Peterson et al. (2019).*

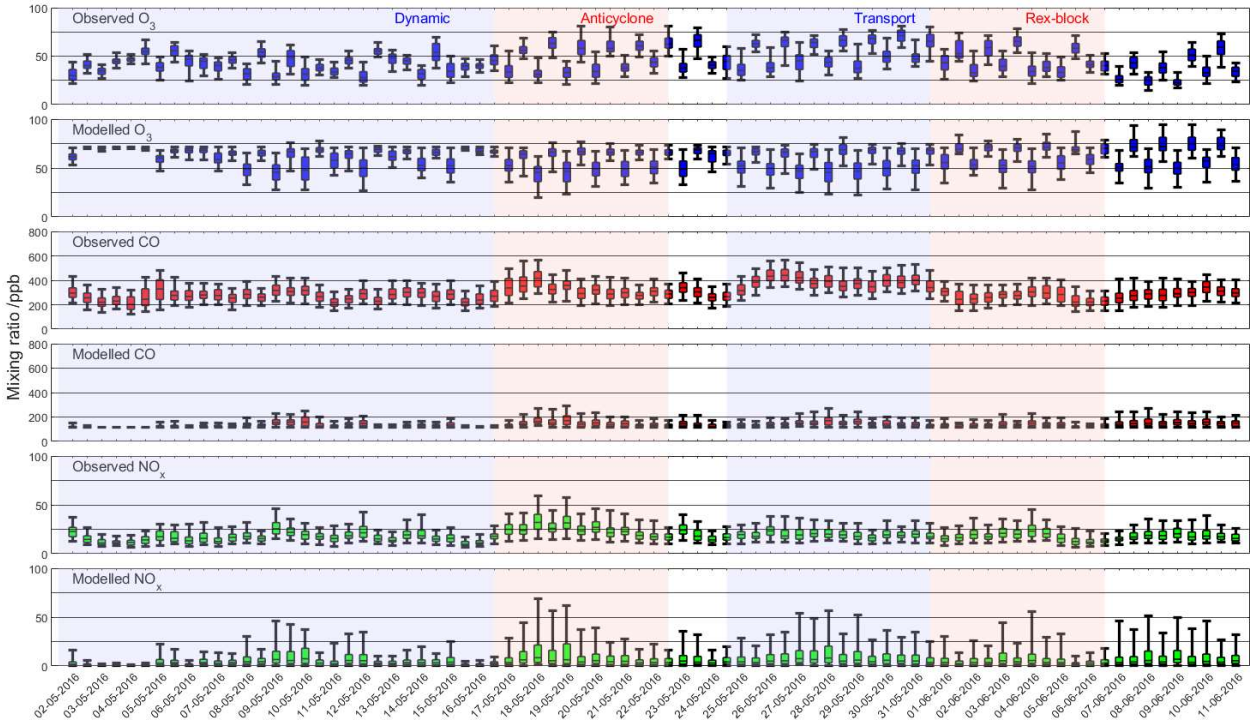

Figure S3: Surface Observation and BL-RL model statistics for O_3 (blue), CO (red), and NO_x (green). *Boxes represent the medians, quartiles, 5th, and 95th percentiles of ozone observations (top) and model output (bottom), where observations were interpolated to the model grid (see Wilson and Prather, 2024). Data were averaged over twelve-hourly intervals between 06:00 and 18:00, and the meteorological stages described by Peterson et al. (2019) are highlighted by blue and red shading.*

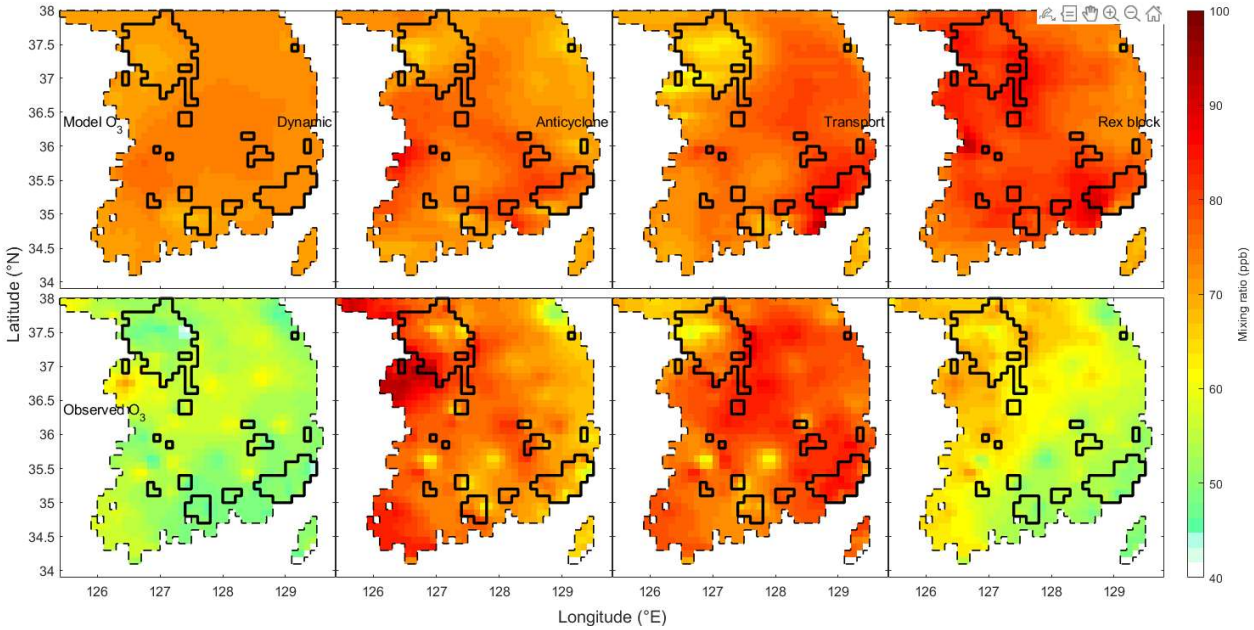

Figure S4: Mean daytime O_3 concentration in the model (top) and gridded observations (bottom). *Grid-cell means were computed between 13:00 and 18:00 during the four meteorological phases (left-to-right): 01-16 May (dynamic), 17-22 May (anticyclone), 25-31 May (transport), and 01-07 June (rex-block). Bold lines enclose grid-cells that were effectively observed by at least five NIER sites during the KORUS-AQ period. Dashed lines enclose the BL-RL model domain*

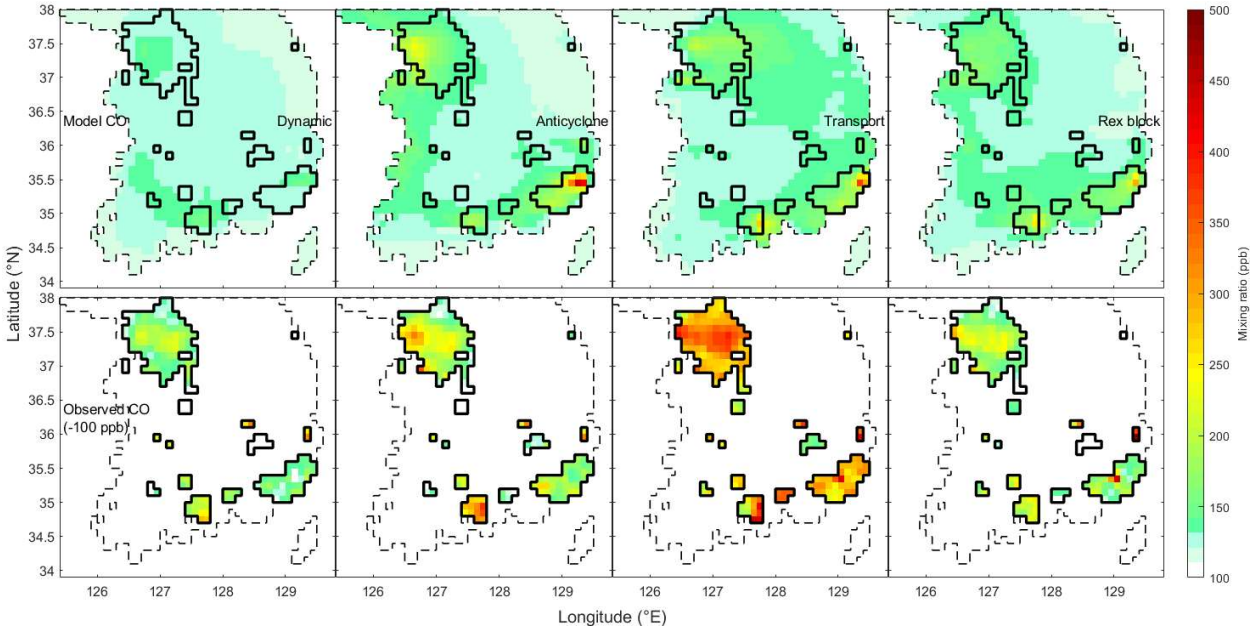

Figure S5: Mean daytime CO concentration in the model (top) and gridded observations (bottom). *As in Figure S4, but for CO. Gridded observations produced from fewer than five effective NIER sites are not shown, and a 100 ppb correction has been subtracted from the observations to better represent DC-8 boundary layer observations (Wilson and Prather, 2024).*

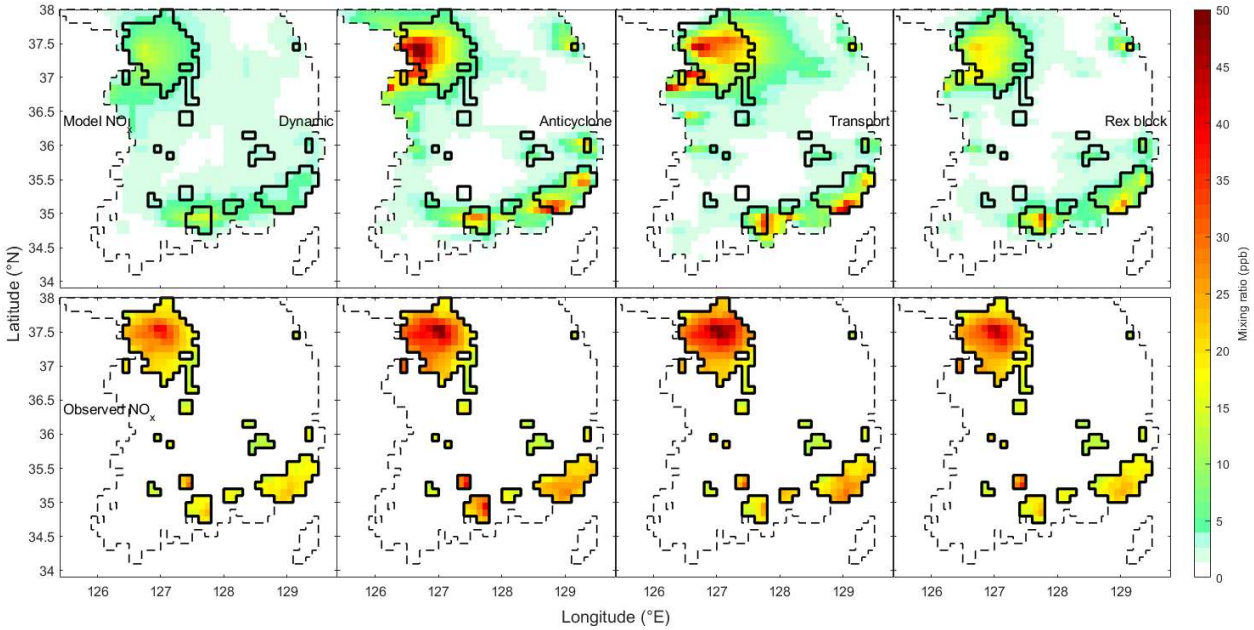

Figure S6: Mean daytime NO_x concentration in the model (top) and gridded observations (bottom). *As in Figure S4, but for NO_x. Gridded observations produced from fewer than five effective NIER sites are not shown.*

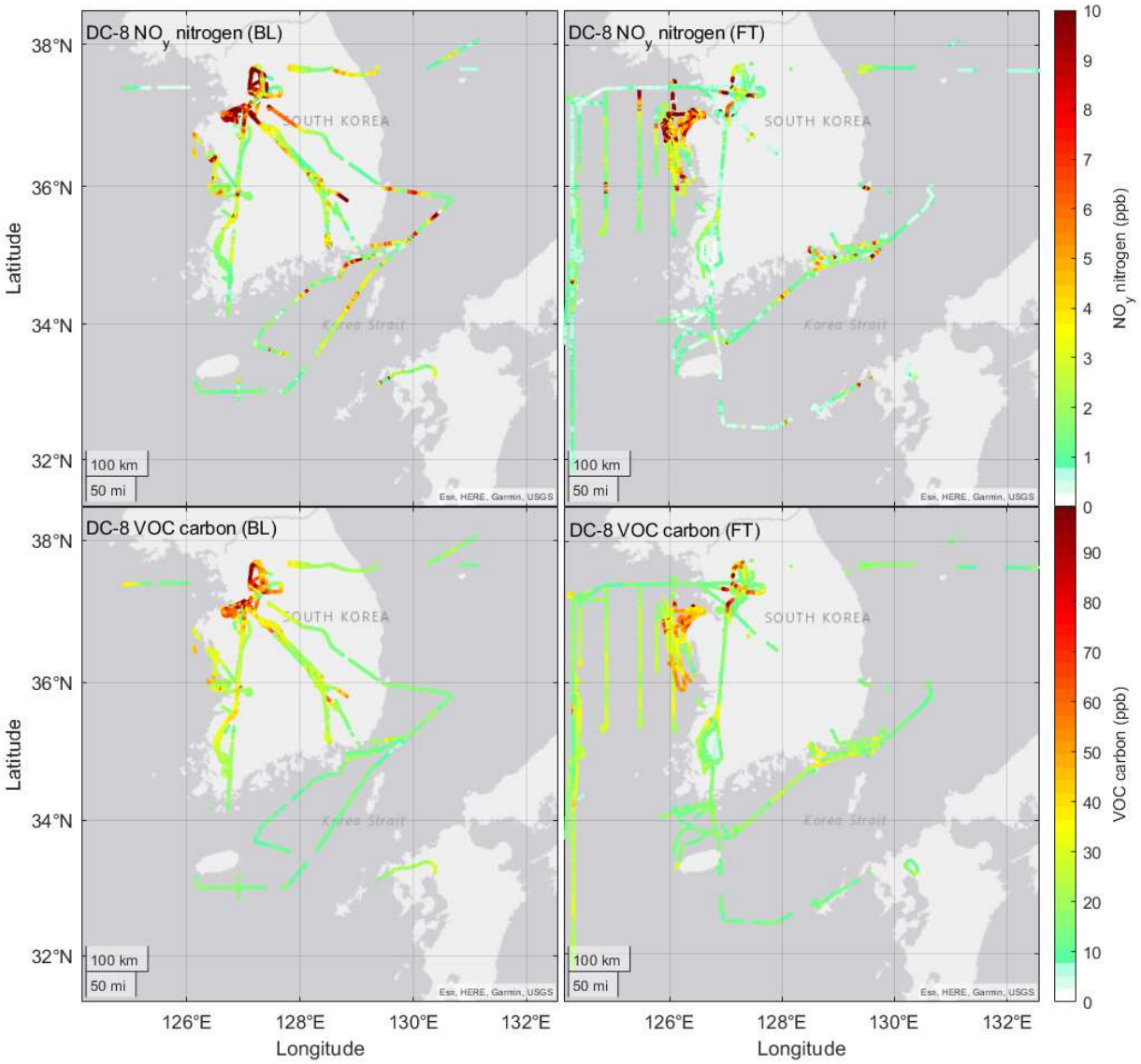

Figure S7: Map of DC-8 observations in the BL (left) and FT (right) coloured by NO_y-nitrogen (top) and VOC-carbon (bottom) mole fraction. *Flight segments (coloured circles) are 10 s merges of 1 Hz KORUS data (KORUS-AQ Science Team, 2019), sampled above (left) and below (right) the hourly, 0.25°x0.25° ERA5 BL height (Hersbach et al., 2023). NO_y includes NO and NO_2 measured by the NCAR four-channel chemiluminescence instrument (Weinheimer et al., 1994) with PAN and PPN from the Georgia Tech Chemical Ionization Mass Spectrometer (GT-CIMS; Huey, 2007). For carbon, VOCs include ethane, benzene, toluene, isoprene, methacrolein, acetaldehyde, acetone, methyl ethyl ketone, and methyl vinyl ketone by Proton Transfer Reaction Mass Spectrometry (PTR-MS; Müller et al., 2014) and formaldehyde by the Compact Atmospheric Multispecies Spectrometer (CAMS; Richter et al., 2015; Spinei et al., 2018).*

S3. Timeline of ozone and methane reactivity

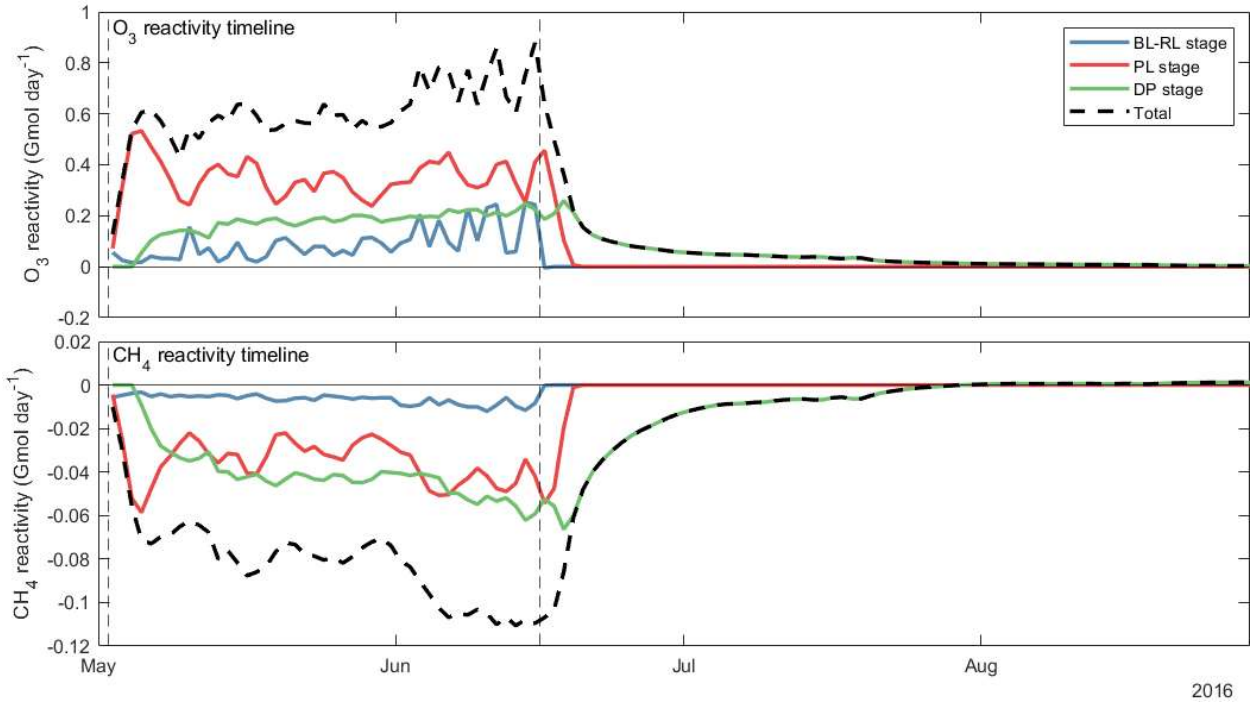

Figure S8: The timeline of O_3 and CH_4 reactivity from 45 days of emissions. *The 45-day emission period is enclosed by dashed lines and is followed by a two-day spin-down period. Ozone and CH_4 reactivities (Gmol day^{-1}) are shown at daily resolution for the BL-RL stage (blue), PL stage (red), and DP stage (green) and integrate to the model stage budgets in Table 9. The BL-RL reactivities are plotted as daily sums over the model domain for CH_4 and over the initial exported plume enhancements for O_3. The PL reactivities are plotted as daily O_3 and CH_4 reactivities in the plumes during aging, synchronised to the timeline according to the plume release times. The DP reactivities are dispersed pollution O_3 and CH_4 changes synchronised to the dispersion of each plume. Daily total reactivities (dashed black line) are the sums of the coloured lines. The spinup of pollution is clear in the first 5 days, and the increasing trends in total reactivities over the next 40 days is driven by the accumulation of DP stage reactivity (green line), and partly by the shift in meteorological conditions in the last 10 days where a longer BL-RL residence time resulted in larger BL-RL reactivities.*

Supplement references

Bloss, C.; Wagner, V.; Jenkin, M. E.; Volkamer, R.; Bloss, W. J.; Lee, J. D.; Heard, D. E.; Wirtz, K.; Martin-Reviejo, M.; Rea, G.; Wenger, J. C.; Pilling, M. J. Development of a Detailed Chemical Mechanism (MCMv3.1) for the Atmospheric Oxidation of Aromatic Hydrocarbons. Atmospheric Chemistry and Physics 2005, 5 (3), 641–664. https://doi.org/10.5194/acp-5-641-2005.

Crippa, M.; Solazzo, E.; Huang, G.; Guizzardi, D.; Koffi, E.; Muntean, M.; Schieberle, C.; Friedrich, R.; Janssens-Maenhout, G. High Resolution Temporal Profiles in the Emissions

Database for Global Atmospheric Research. Sci Data 2020, 7 (1), 121. https://doi.org/10.1038/s41597-020-0462-2.

Hersbach, H., Bell, B., Berrisford, P., Biavati, G., Horányi, A., Muñoz Sabater, J., Nicolas, J., Peubey, C., Radu, R., Rozum, I., Schepers, D., Simmons, A., Soci, C., Dee, D., Thépaut, J-N. (2023): ERA5 hourly data on single levels from 1940 to present. Copernicus Climate Change Service (C3S) Climate Data Store (CDS), DOI: 10.24381/cds.adbb2d47 (Accessed on 26-Feb-2025)

Huey, L. G. Measurement of Trace Atmospheric Species by Chemical Ionization Mass Spectrometry: Speciation of Reactive Nitrogen and Future Directions. Mass Spectrometry Reviews 2007, 26 (2), 166–184. https://doi.org/10.1002/mas.20118.

Jenkin, M. E.; Saunders, S. M.; Pilling, M. J. The Tropospheric Degradation of Volatile Organic Compounds: A Protocol for Mechanism Development. Atmospheric Environment 1997, 31 (1), 81–104. https://doi.org/10.1016/S1352-2310(96)00105-7.

Jenkin, M. E.; Saunders, S. M.; Wagner, V.; Pilling, M. J. Protocol for the Development of the Master Chemical Mechanism, MCM v3 (Part B): Tropospheric Degradation of Aromatic Volatile Organic Compounds. Atmospheric Chemistry and Physics 2003, 3 (1), 181–193. https://doi.org/10.5194/acp-3-181-2003.

Jenkin, M. E.; Young, J. C.; Rickard, A. R. The MCM v3.3.1 Degradation Scheme for Isoprene. Atmospheric Chemistry and Physics 2015, 15 (20), 11433–11459. https://doi.org/10.5194/acp-15-11433-2015.

KORUS-AQ Science Team: KORUS-AQ NASA DC-8 airborne 10 s merged data revision 6 - ICARTT Files, NASA Langley Atmospheric Science Data Center DAAC [data set], https://doi.org/10.5067/Suborbital/KORUSAQ/DATA01, 2019.

Müller, M.; Mikoviny, T.; Feil, S.; Haidacher, S.; Hanel, G.; Hartungen, E.; Jordan, A.; Märk, L.; Mutschlechner, P.; Schottkowsky, R.; Sulzer, P.; Crawford, J. H.; Wisthaler, A. A Compact PTR-ToF-MS Instrument for Airborne Measurements of Volatile Organic Compounds at High Spatiotemporal Resolution. Atmospheric Measurement Techniques 2014, 7 (11), 3763–3772. https://doi.org/10.5194/amt-7-3763-2014.

Peterson, D. A.; Hyer, E. J.; Han, S.-O.; Crawford, J. H.; Park, R. J.; Holz, R.; Kuehn, R. E.; Eloranta, E.; Knote, C.; Jordan, C. E.; Lefer, B. L. Meteorology Influencing Springtime Air Quality, Pollution Transport, and Visibility in Korea. Elementa: Science of the Anthropocene 2019, 7, 57. https://doi.org/10.1525/elementa.395.

Richter, D.; Weibring, P.; Walega, J. G.; Fried, A.; Spuler, S. M.; Taubman, M. S. Compact Highly Sensitive Multi-Species Airborne Mid-IR Spectrometer. Appl. Phys. B 2015, 119 (1), 119–131. https://doi.org/10.1007/s00340-015-6038-8.

Saunders, S. M.; Jenkin, M. E.; Derwent, R. G.; Pilling, M. J. Protocol for the Development of the Master Chemical Mechanism, MCM v3 (Part A): Tropospheric Degradation of Non-Aromatic Volatile Organic Compounds. Atmospheric Chemistry and Physics 2003, 3 (1), 161–180. https://doi.org/10.5194/acp-3-161-2003.

Spinei, E.; Whitehill, A.; Fried, A.; Tiefengraber, M.; Knepp, T. N.; Herndon, S.; Herman, J. R.; Müller, M.; Abuhassan, N.; Cede, A.; Richter, D.; Walega, J.; Crawford, J.; Szykman, J.; Valin, L.; Williams, D. J.; Long, R.; Swap, R. J.; Lee, Y.; Nowak, N.; Poche, B. The First Evaluation of Formaldehyde Column Observations by Improved Pandora Spectrometers during the KORUS-AQ Field Study. Atmospheric Measurement Techniques 2018, 11 (9), 4943–4961. https://doi.org/10.5194/amt-11-4943-2018.

Wilson, C. P.; Prather, M. J. Gridded Surface O3, NOx, and CO Abundances for Model Metrics from the South Korean Ground Station Network. Atmospheric Measurement Techniques 2025, 18 (8), 1757–1769. https://doi.org/10.5194/amt-18-1757-2025.

Woo, J.-H.; Kim, Y.; Kim, H.-K.; Choi, K.-C.; Eum, J.-H.; Lee, J.-B.; Lim, J.-H.; Kim, J.; Seong, M. Development of the CREATE Inventory in Support of Integrated Climate and Air Quality Modeling for Asia. Sustainability 2020, 12 (19), 7930. https://doi.org/10.3390/su12197930.